

The Effect of Rotation on Double Diffusive Convection: Perspectives from Linear Stability Analysis

YU LIANG,^a JEFFREY R. CARPENTER,^b AND MARY-LOUISE TIMMERMANS^a

^a *Department of Earth and Planetary Sciences, Yale University, New Haven, Connecticut*

^b *Institute of Coastal Ocean Dynamics, Helmholtz-Zentrum Hereon, Geesthacht, Germany*

(Manuscript received 18 March 2021, in final form 13 August 2021)

ABSTRACT: Diffusive convection can occur when two constituents of a stratified fluid have opposing effects on its stratification and different molecular diffusivities. This form of convection arises for the particular temperature and salinity stratification in the Arctic Ocean and is relevant to heat fluxes. Previous studies have suggested that planetary rotation may influence diffusive–convective heat fluxes, although the precise physical mechanisms and regime of rotational influence are not well understood. A linear stability analysis of a temperature and salinity interface bounded by two mixed layers is performed here to understand the stability properties of a diffusive–convective system, and in particular the transition from nonrotating to rotationally controlled heat transfer. Rotation is shown to stabilize diffusive convection by increasing the critical Rayleigh number to initiate instability. In the rotationally controlled regime, a $-4/3$ power law is found between the critical Rayleigh number and the Ekman number, similar to the scaling for rotating thermal convection. The transition from nonrotating to rotationally controlled convection, and associated drop in heat fluxes, is predicted to occur when the thermal interfacial thickness exceeds about 4 times the Ekman layer thickness. A vorticity budget analysis indicates how baroclinic vorticity production is counteracted by the tilting of planetary vorticity by vertical shear, which accounts for the stabilization effect of rotation. Finally, direct numerical simulations yield generally good agreement with the linear stability analysis. This study, therefore, provides a theoretical framework for classifying regimes of rotationally controlled diffusive–convective heat fluxes, such as may arise in some regions of the Arctic Ocean.

KEYWORDS: Diffusion; Diapycnal mixing; Numerical analysis/modeling

1. Introduction

Double diffusion is a type of convection that may occur when two constituents of a stably stratified fluid have opposing density stratification and different molecular diffusivities (Radko 2013). The classic example is oceanic double diffusion that can be active for certain temperature and salinity stratifications because thermal diffusivity is approximately 100 times larger than the diffusivity of salt (e.g., Schmitt 1994). One mode of double diffusion, known as diffusive convection, can arise when temperature and salinity both increase with depth. Consider, for example, a relatively cold and fresh water layer overlying a (more dense) relatively warm and salty layer (Turner and Stommel 1964). Between the two layers the diffusive thermal interface grows faster than the haline interface. This sets up the formation of gravitationally unstable diffusive boundary layers at the edges of the interface (Fig. 1), and when conditions are favorable, convection is triggered. The subsequent vertical fluxes of heat and salt across the interface are of primary interest, and a number of parameterizations for diffusive–convective fluxes have been developed (e.g., Turner 1965; Linden and Shirtcliffe 1978; Kelley 1990; Flanagan et al. 2013). Note that the heat and salt of the oceanic setting can be replaced by any two fluid constituents (i.e., a two-component system) that have different diffusivities, and double diffusion has been studied in a variety of other settings, including planetary interiors and stellar evolution (see, e.g., Radko 2013).

The Arctic Ocean, characterized by relatively cool and fresh water overlying relatively warm and salty water, presents a well-recognized example of diffusive convection at middepth in its water column (e.g., Neal et al. 1969; Neshyba et al. 1971; Padman and Dillon 1987; Timmermans et al. 2008; Guthrie et al. 2015). The process manifests itself as stacked layers, each of uniform temperature and salinity, separated by relatively thin high-gradient interfaces—a diffusive–convective staircase. Diffusive convection is an important mechanism for transporting heat from the deeper, warmer ocean layers toward the surface ocean and overlying sea ice (e.g., Polyakov et al. 2012; Carmack et al. 2015). Reliable parameterized estimates of these heat fluxes are needed where turbulence observations are sparse and logistically challenging to acquire. Planetary rotation, however, is usually not accounted for in heat flux parameterizations, although its influence may be important in certain settings (Kelley 1987; Carpenter and Timmermans 2014). In particular, Carpenter and Timmermans (2014) found that the influence of planetary rotation may limit double-diffusive heat fluxes in some regions of the Arctic Ocean where staircase interfaces are relatively thick. In this study, we explore the influence of Earth’s rotation on diffusive–convective heat fluxes. For direct comparison with the results of Carpenter and Timmermans (2014), who considered the Arctic setting in particular, in our analysis we use parameters consistent with those that characterize the Arctic Ocean’s diffusive–convective staircase.

Past studies have shown that planetary rotation can inhibit pure thermal convection and the associated heat fluxes (e.g., Chandrasekhar 1953; Niiler and Bisshopp 1965; Rossby 1969; King et al. 2012). This is explained as a result of the

Corresponding author: Yu Liang, yu.liang@yale.edu

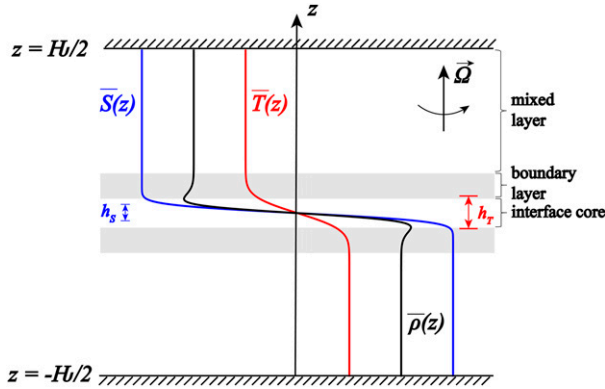


FIG. 1. Schematic of a diffusive-convective interface. Red and blue lines indicate background temperature and salinity profiles, and the black line indicates the background density. Horizontal gray bars mark the gravitationally unstable boundary layers, which are bounded by specified values of vertical gradients of background density (see text). The mixed layer in the top half of the domain and the stable interface core are also marked; h_T and h_S are temperature and salinity interfacial thicknesses, respectively.

suppression of vertical motion through the Taylor-Proudman effect (Chandrasekhar 2013). Considering measurements from rotating thermal convection experiments, Kelley (1987) derived an empirical criterion to indicate when diffusive-convective heat fluxes may be affected by rotation. Carpenter and Timmermans (2014) reformulated Kelley's condition in terms of the relative thicknesses of the Ekman layer and the thermal interface, and tested this via direct numerical simulation (DNS) of diffusive convection. Their simulations provided support for Kelley's results, demonstrating that heat fluxes can be strongly inhibited by rotation when the thickness of the thermal interface is around 5 times the thickness of the Ekman boundary layer. A precise physical interpretation of this transition remains to be described.

In this study, we examine the linear stability properties of a double-diffusive system, with a focus on the diffusive-convective mode, to understand the transition to rotationally controlled heat transfer. Instability of a double-diffusive system was first shown via linear stability analysis (LSA) applied to a fluid layer characterized by linear background temperature and salinity stratification (Stern 1960; Veronis 1965; Nield 1967; Baines and Gill 1969; Pearlstein 1981). Compared to this system, diffusive-convective staircases, characterized by sharp interfaces in temperature and salinity that are bounded by two mixed layers (Fig. 1), have been shown to have considerably different linear stability properties (Carpenter et al. 2012b; Smyth and Carpenter 2019). Here, we extend the analysis of Carpenter et al. (2012b) to include the effects of planetary rotation in a LSA, and examine for what regime and how rotation influences diffusive convection. We show that physical insights into the effects of rotation on diffusive-convective heat fluxes can be gained through examination of the LSA solutions.

The paper is organized as follows. In the next section, we formulate and solve the LSA, showing consistency with the Kelley condition for the transition from the nonrotating to

the rotationally controlled regime for diffusive-convective heat fluxes. We then examine the LSA solutions in the context of the vorticity balance to demonstrate the mechanism by which the influence of rotation inhibits the vertical transfer of properties. In section 3, we validate our LSA-based transition criterion using DNS, and summarize and discuss our results in section 4. While we explore a parameter regime relevant to diffusive convection in the Arctic Ocean, our approach and findings may be generalized to other diffusive-convective settings.

2. Linear stability analysis

a. Formulation and solution

We consider a three-dimensional Boussinesq fluid layer of infinite horizontal extent on an f plane (i.e., with a fixed rate of rotation). Let T and S be temperature and salinity, respectively, such that density ρ may be written as

$$\rho = \rho_0[1 + \beta(S - S_0) - \alpha(T - T_0)], \quad (1)$$

where ρ_0 , T_0 , and S_0 are reference values for density, temperature, and salinity, respectively, and thermal expansion coefficient α and haline contraction coefficient β are assumed to be constant. Conservation of momentum and mass are given by

$$\frac{\partial \mathbf{v}}{\partial t} + \mathbf{v} \cdot \nabla \mathbf{v} = -\frac{1}{\rho_0} \nabla p + \frac{\rho}{\rho_0} \mathbf{g} + \nu \nabla^2 \mathbf{v} - 2\mathbf{\Omega} \times \mathbf{v}, \quad (2)$$

$$\nabla \cdot \mathbf{v} = 0, \quad (3)$$

where $\mathbf{v} = (u, v, w)$ is the three-dimensional velocity vector, p is pressure, $\mathbf{g} = (0, 0, -g)$ is gravitational acceleration, ν is molecular viscosity, and $\mathbf{\Omega} = (0, 0, f/2)$ is the vertical angular velocity where f is the Coriolis parameter. Advection-diffusion equations for T and S are given by

$$\frac{\partial T}{\partial t} + \mathbf{v} \cdot \nabla T = \kappa_T \nabla^2 T, \quad (4)$$

$$\frac{\partial S}{\partial t} + \mathbf{v} \cdot \nabla S = \kappa_S \nabla^2 S, \quad (5)$$

where κ_T and κ_S are the molecular diffusivities of temperature and salinity, respectively.

Let us consider perturbations about a motionless background state and write

$$T = \bar{T} + \tilde{T}, \quad S = \bar{S} + \tilde{S}, \quad \rho = \bar{\rho} + \tilde{\rho}, \quad \mathbf{v} = \tilde{\mathbf{v}}, \quad p = \bar{p} + \tilde{p}, \quad (6)$$

where the tilde indicates perturbation quantities from the background states denoted by overbars. The background pressure is hydrostatic and the background density profile can be written as

$$\bar{\rho}(z) = \rho_0 \{1 + \beta[\bar{S}(z) - S_0] - \alpha[\bar{T}(z) - T_0]\}. \quad (7)$$

The vertical structure of the $\bar{T}(z)$ and $\bar{S}(z)$ profiles will be chosen to resemble the layer and interface structure that is present in diffusive convective staircases, as shown in Fig. 1.

We substitute (6) into the governing equations and linearize to obtain

$$\frac{\partial \tilde{\xi}}{\partial t} - \nu \nabla^2 \tilde{\xi} - 2\Omega \frac{\partial \tilde{w}}{\partial z} = 0, \quad (8)$$

$$\left(\frac{\partial}{\partial t} - \nu \nabla^2 \right) \nabla^2 \tilde{w} + 2\Omega \frac{\partial \tilde{\xi}}{\partial z} + g \nabla_h^2 (\beta \tilde{S} - \alpha \tilde{T}) = 0, \quad (9)$$

$$\frac{\partial \tilde{T}}{\partial t} + \tilde{w} \frac{\partial \bar{T}}{\partial z} - \kappa_T \nabla^2 \tilde{T} = 0, \quad (10)$$

$$\frac{\partial \tilde{S}}{\partial t} + \tilde{w} \frac{\partial \bar{S}}{\partial z} - \kappa_S \nabla^2 \tilde{S} = 0, \quad (11)$$

where $\tilde{\xi} = \partial \tilde{v} / \partial x - \partial \tilde{u} / \partial y$ is the vertical component of relative vorticity and $\nabla_h^2 = \partial^2 / \partial x^2 + \partial^2 / \partial y^2$. Note that here we assume the background temperature and salinity (\bar{T}, \bar{S}) do not diffuse with time, which has important consequences for the nature of the instability, and for the results of this study. We discuss this assumption in greater detail later in the paper (see also Carpenter et al. 2012b for a discussion).

It is convenient to nondimensionalize this system. We first introduce the thermal interfacial thickness h_T and the haline interfacial thickness h_S

$$h_T = \left| \Delta T \left/ \frac{\partial \bar{T}}{\partial z} \right|_{z=0} \right|, \quad h_S = \left| \Delta S \left/ \frac{\partial \bar{S}}{\partial z} \right|_{z=0} \right| \quad (12)$$

where $z = 0$ indicates that the derivative is calculated at the center of the interface (see Fig. 1) and $||$ indicates the absolute value. Temperature and salinity scales ΔT and ΔS are the temperature and salinity differences across the diffusive interface, respectively.

A velocity scale κ_T / h_T and a time scale h_T^2 / κ_T can be defined in terms of the thermal interfacial thickness h_T . Nondimensionalizing (8)–(11) yields (asterisks denote nondimensional variables):

$$\frac{\partial \xi_*}{\partial t_*} - \text{Pr} \nabla_*^2 \xi_* - \frac{\text{Pr}}{\text{Ek}_I} \frac{\partial w_*}{\partial z_*} = 0, \quad (13)$$

$$\left(\frac{1}{\text{Pr}} \frac{\partial}{\partial t_*} - \nabla_*^2 \right) \nabla_*^2 w_* + \frac{1}{\text{Ek}_I} \frac{\partial \xi_*}{\partial z_*} + \text{Ra}_I \nabla_h^2 (R_\rho S_* - T_*) = 0, \quad (14)$$

$$\frac{\partial T_*}{\partial t_*} + w_* \frac{\partial \bar{T}}{\partial z_*} - \nabla_*^2 T_* = 0, \quad (15)$$

$$\frac{\partial S_*}{\partial t_*} + w_* \frac{\partial \bar{S}}{\partial z_*} - \tau \nabla_*^2 S_* = 0, \quad (16)$$

where $\text{Ek}_I = \nu / (2\Omega h_T^2)$ and $\text{Ra}_I = g \alpha \Delta T h_T^3 / (\nu \kappa_T)$ are interfacial Ekman and Rayleigh numbers, $\text{Pr} = \nu / \kappa_T$ is the Prandtl number, $\tau = \kappa_S / \kappa_T$, and $R_\rho = \beta \Delta S / (\alpha \Delta T)$ are diffusivity and density ratios.

Following Carpenter et al. (2012b), we consider background temperature and salinity profiles described by error functions:

$$\begin{aligned} \bar{T}_*(z_*) &= T_0 / \Delta T - \text{erf}(\sqrt{\pi} z_*) / 2 \quad \text{and} \\ \bar{S}_*(z_*) &= S_0 / \Delta S - \text{erf}(\sqrt{\pi} r z_*) / 2 \quad \left(-\frac{H}{2} \leq z_* \leq \frac{H}{2} \right), \end{aligned} \quad (17)$$

where $r = h_T / h_S$ is the ratio of thermal to haline interfacial thicknesses ($r > 1$), and $H = \mathcal{H} / h_T$ is the dimensionless domain height for a domain height \mathcal{H} . These background profiles delineate distinct regions of the fluid layer: a stable interface core, unstable boundary layers, and mixed layers (Fig. 1).

We take the boundaries of the domain ($z_* = \pm H/2$) to be rigid-lid, free slip and constant temperature and salinity such that the following conditions apply on these boundaries: $w_* = \partial^2 w_* / \partial z_*^2 = \partial \xi_* / \partial z_* = T_* = S_* = 0$. Solutions are assumed to take the form

$$\{w_*, T_*, S_*\} = \sum_{n=1}^N \{\hat{w}_n, \hat{T}_n, \hat{S}_n\} \sin \left[\frac{n\pi(z_* + H/2)}{H} \right] \times \exp(ik_* x_* + il_* y_* + \sigma_* t_*), \quad (18)$$

$$\xi_* = \sum_{n=1}^N \hat{\xi}_n \cos \left[\frac{n\pi(z_* + H/2)}{H} \right] \exp(ik_* x_* + il_* y_* + \sigma_* t_*), \quad (19)$$

where $\{\hat{w}_n, \hat{T}_n, \hat{S}_n, \hat{\xi}_n\}$ are nondimensional coefficients in the series expansion of each vertical normal mode, k_* and l_* are horizontal wavenumbers (nondimensionalized by h_T^{-1}), and $\sigma_* = \sigma_{r*} + i\sigma_{i*}$ is the complex growth rate (nondimensionalized by κ_T / h_T^2). We use a Fourier–Galerkin method of solution, which can be constructed as follows (see more details in Smyth and Carpenter 2019). Introduce the function $\beta_n(z_*) = \sin[n\pi(z_* + H/2)/H]$ and define the integral operator

$$\langle \beta_n(z_*) \rangle = \frac{2}{H} \int_{-H/2}^{H/2} \beta_n(z_*) dz_*. \quad (20)$$

Using the identity $\langle \beta_n(z_*) \beta_m(z_*) \rangle = (2/H) \int_{-H/2}^{H/2} \beta_n(z_*) \beta_m(z_*) dz_* = \delta_{nm}$, we substitute (18) and (19) into (13)–(16) and integrate over the vertical domain to yield

$$\sigma_* \hat{\xi}_n = -\alpha_n^2 \text{Pr} \hat{\xi}_n + \frac{\text{Pr}}{\text{Ek}_I} \frac{n\pi}{H} \hat{w}_n, \quad (21)$$

$$\sigma_* \hat{w}_n = -\frac{\text{Pr}}{\text{Ek}_I} \frac{n\pi}{H \alpha_n^2} \hat{\xi}_n - \text{Pr} \alpha_n^2 \hat{w}_n - \text{Ra}_I \text{Pr} \frac{K_*^2}{\alpha_n^2} (R_\rho \hat{S}_n - \hat{T}_n), \quad (22)$$

$$\sigma_* \hat{T}_n = -\sum_{m=1}^N \hat{w}_m \left\langle \beta_n(z_*) \beta_m(z_*) \frac{\partial \bar{T}}{\partial z_*} \right\rangle - \alpha_n^2 \hat{T}_n, \quad (23)$$

$$\sigma_* \hat{S}_n = -\sum_{m=1}^N \hat{w}_m \left\langle \beta_n(z_*) \beta_m(z_*) \frac{\partial \bar{S}}{\partial z_*} \right\rangle - \tau \alpha_n^2 \hat{S}_n. \quad (24)$$

Here, we define $K_*^2 = k_*^2 + l_*^2$ and $\alpha_n^2 = K_*^2 + (n\pi/H)^2$. These four equations constitute an eigenvalue problem $\mathbf{AX} = \sigma_* \mathbf{X}$,

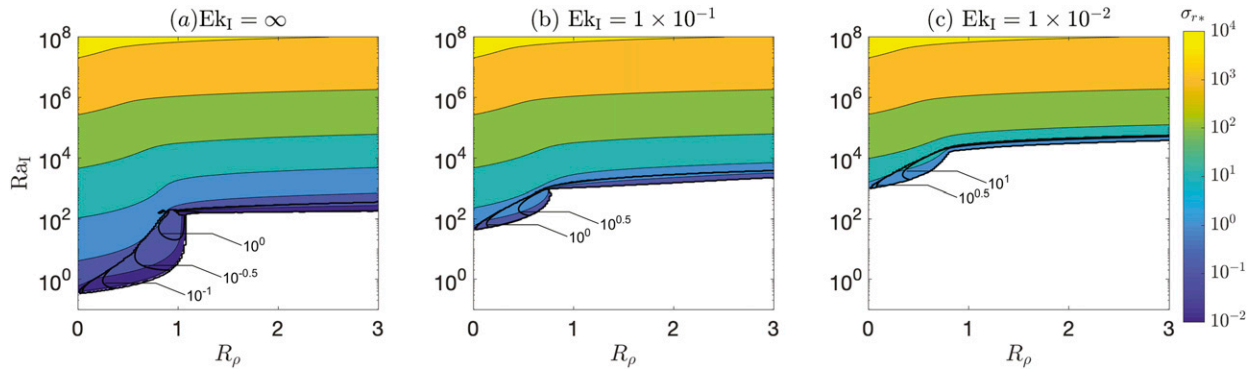


FIG. 2. Positive growth rates of the most unstable mode on the R_ρ – Ra_I plane for $H = 10$, $r = 2$ and (a) $Ek_I = \infty$, the nonrotating case, and rotating cases (b) $Ek_I = 10^{-1}$ and (c) $Ek_I = 10^{-2}$. Thin contours and color shading indicate the nondimensional linear growth rate σ_{r*} , and thick contour lines indicate the nondimensional oscillatory frequency σ_{i*} .

for eigenvector \mathbf{X} of length $4N$ created by concatenating the Fourier coefficients $\{\hat{\xi}_n, \hat{w}_n, \hat{T}_n, \hat{S}_n\}$. The \mathbf{A} is a matrix of size $4N \times 4N$, and σ_* is the eigenvalue. The solutions vary with K_* and other dimensionless parameters including Ek_I , Ra_I , R_ρ , r , and H . The complex growth rate σ_* and corresponding coefficients $\{\hat{\xi}_n, \hat{w}_n, \hat{T}_n, \hat{S}_n\}$ of the most unstable mode may be determined (given values of Ek_I , Ra_I , R_ρ , r , and H) by solving the eigenvalue problem (we take $N = 100$). We take $Pr = 6.25$ and $\tau = 0.01$, which we use later in the DNS for comparison with Carpenter and Timmermans (2014).

b. Stability diagrams

The stability diagrams of Fig. 2 show positive unstable growth rates, σ_{r*} , of the most unstable mode on the R_ρ – Ra_I plane, for fixed values of $r = 2$ and $H = 10$. In addition, the oscillation frequency σ_{i*} of the fastest growing mode is also shown (thick contours). Our choices for the ratio r of thermal to haline interfacial thicknesses, and the dimensionless domain height H , are taken to be consistent with the observations and simulations of Sommer et al. (2013, 2014) and Carpenter et al. (2012a). The stability diagrams for nonrotating ($Ek_I = \infty$) and rotating ($Ek_I = 0.1, 0.01$) cases share some general features: For any fixed R_ρ , the system is stable at low Ra_I , then becomes oscillatory unstable (i.e., $\sigma_{r*} > 0$ and $\sigma_{i*} \neq 0$) and finally convectively unstable (i.e., $\sigma_{r*} > 0$ and $\sigma_{i*} = 0$) with increasing Ra_I . That the system is oscillatory unstable at the stability boundary ($\sigma_{r*} = 0$) is consistent with previous analyses that considered linear temperature and salinity gradients (Stern 1960; Veronis 1965; Nield 1967; Baines and Gill 1969; Pearlstein 1981). The stability diagrams appear to be separated by R_ρ into two regions: for the nonrotating case (Fig. 2a) for example, one region for $R_\rho < R_\rho^*$ [with $R_\rho^* = (Pr + 1)/(Pr + \tau)$; see Veronis 1965; Carpenter et al. 2012b] that is characterized by an oscillatory regime that extends over a broader range of Ra_I , and the other for $R_\rho > R_\rho^*$ that has a narrower oscillatory regime and instability at larger Ra_I . Carpenter et al. (2012b) showed that the two regions have unstable modes with different vertical structures: the region of smaller R_ρ (i.e., $R_\rho < R_\rho^*$ in Fig. 2a) is characterized by the interfacial unstable mode whose perturbations are

the strongest at the center of the interface, while the region of higher R_ρ (i.e., $R_\rho > R_\rho^*$ in Fig. 2a) is characterized by the boundary layer unstable mode whose perturbations are the strongest at the gravitationally unstable boundary layers. Instability within the smaller R_ρ region is the interfacial analog of the instability of linear profiles (e.g., Stern 1960; Baines and Gill 1969) acting within the interface center, and a convective-type instability will only grow for sufficiently large Ra_I such that viscosity and diffusion can be overcome; whereas the larger R_ρ region is associated with gravitationally unstable boundary layers and requires $r > 1$. It is this large R_ρ unstable region that is relevant for Arctic Ocean diffusive convection, since Arctic Ocean staircases typically have $2 < R_\rho < 10$ (Shibley et al. 2017), and we expect this boundary layer unstable mode to trigger instability for staircases with and without the effects of rotation. We therefore confine our attention to the boundary layer modes throughout this paper.

With respect to the influence of rotation, it can be seen that the value of Ra_I at the stability boundary is significantly larger, and the growth rate at the same Ra_I is smaller, in the rotating (Figs. 2b,c) versus the nonrotating (Fig. 2a) case. This suggests that rotation inhibits the onset of diffusive convection and stabilizes the system. Finally, it is of note that nonrotating and rotating cases are indistinguishable for $Ra_I > 10^6$, indicating that for large Ra_I , weak rotation does not affect the linear stability properties of a staircase. Next, we examine how a critical interfacial Rayleigh number (characterizing the onset of instability) depends upon the strength of rotational effects, characterized by the interfacial Ekman number.

c. Quantifying the effects of rotation

In quantifying the effects of rotation on diffusive–convective fluxes, we seek a critical interfacial Rayleigh number, Ra_I^c , that describes when the boundary layer first becomes unstable. This is normally described by the condition that the growth rate becomes positive, i.e., $\sigma_{r*} > 0$. However, due to our neglect of the unsteady growth of the background temperature and salinity profiles in time, we require that the growth rate of the instability must sufficiently exceed that of the profiles, in order for the assumption of a steady background to be valid (see e.g.,

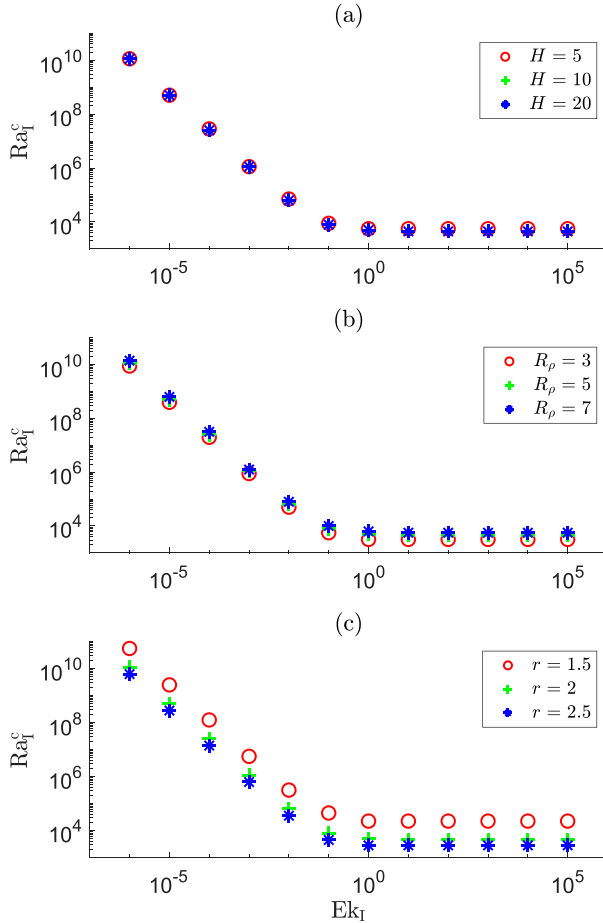


FIG. 3. The critical interfacial Rayleigh number Ra_I^c (where $\sigma_{r*} = 2\pi$, see text) as a function of the interfacial Ekman number Ek_I for (a) $r = 2$, $R_\rho = 5$, and varying H ; (b) $r = 2$, $H = 10$, and varying R_ρ ; (c) $H = 10$, $R_\rho = 5$, and varying r . In each case, the instability is influenced by rotation in the region $Ek_I \lesssim 0.1$.

discussion by Smyth and Carpenter 2019). We therefore define a critical threshold by requiring that the perturbation growth rate exceeds that of the profiles, determined by Carpenter et al. (2012b) to be $\sigma_{r*} = 2\pi$ for error function profiles, with the understanding that this is an approximate criterion. With this constraint, Ra_I^c is calculated over a range of Ek_I for different combinations of H , R_ρ , and r (Fig. 3). It can be seen that the Ra_I^c – Ek_I relationship is similar among each group of parameters: When the influence of rotation is sufficiently small ($Ek_I \gtrsim 1$), Ra_I^c remains independent of the rotation strength (i.e., independent of Ek_I). In a rotationally controlled regime ($Ek_I \lesssim 0.1$), there exists a distinct power law relationship between Ra_I^c and Ek_I . For each set of parameters considered, a least squares fit yields $Ra_I^c \propto Ek_I^{-4/3}$, in agreement with previous LSA using linear background temperature and salinity profiles (see Pearlstein 1981) and with the scaling for single-component convection with linear background temperature profiles (see Chandrasekhar 1953). That is, even for profiles exhibiting an interface, the Ra_I^c – Ek_I relationship follows the $-4/3$ power law.

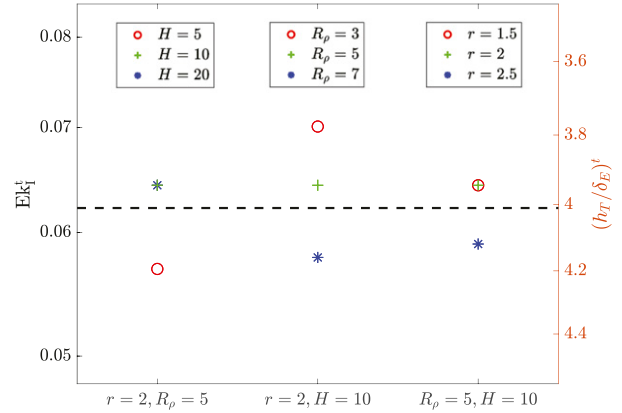


FIG. 4. The transition value of the interfacial Ekman number Ek_I^t (left axis) and the corresponding ratio of thermal interfacial thickness to Ekman layer thickness $(h_T/\delta_E)^t$ (right axis) between the nonrotating and rotationally controlled regimes for the parameters labeled on the x axis. For each set of symbols (in each of the three columns), the legends denote the corresponding parameter values. The black dashed line indicates the mean transition values of Ek_I^t and $(h_T/\delta_E)^t$.

We note that for rotating thermal convection with linear background temperature profiles, the most unstable normal mode of each perturbation variable consists of only the fundamental $n = 1$ Fourier component (i.e., the perturbation is strongest at the center of the interface; see Chandrasekhar 2013). In the limit $Ek_I \rightarrow 0$, Chandrasekhar (2013) found analytically that the asymptotic dependence of Ra_I^c on Ek_I yields the $-4/3$ power law. In the setting described here however, the most unstable normal mode consists of more than one vertical Fourier component, and the eigenvalue problem cannot be easily simplified. Still, the same dependence of Ra_I^c on Ek_I is found, suggesting that the $-4/3$ power law may hold for a range of background density profiles under the influence of rotation, and not just for linear profiles. We can also compute the critical horizontal wavenumber K_*^c corresponding to Ra_I^c ; this yields the scaling $K_*^c \propto Ek_I^{-1/3}$ (not shown), also in agreement with the scaling for thermal convection with linear background temperature profiles (Chandrasekhar 1953).

We can calculate a value of Ek_I characterizing the transition between nonrotating and rotationally controlled regimes by intersecting the fit in the rotationally controlled regime with the nonrotating value of Ra_I^c for each set of parameters. For our considered range of parameters, which are representative of diffusive convective staircases in the Arctic Ocean (Shibley et al. 2017), the mean value of this transition interfacial Ekman number is 0.062 ± 0.005 , relatively insensitive to variations in r , R_ρ , and H (Fig. 4). Recall that $Ek_I = \nu/(2\Omega h_T^2) = \delta_E^2/h_T^2$, where $\delta_E = \sqrt{\nu/2\Omega}$ is the vertical scale of the frictional Ekman layer. Therefore, we can relate the transition to a value of h_T/δ_E , the ratio of thermal interfacial thickness to Ekman layer thickness. This yields a transition value of $(h_T/\delta_E)^t \approx 4.0$, which suggests that if the thermal interfacial thickness exceeds about 4 times the Ekman layer thickness, diffusive convection falls into the rotationally controlled regime and diffusive–convective heat fluxes are expected to be inhibited.

Kelley (1987) analyzed heat flux measurements from the rotating thermal convection experiments of Rossby (1969) in the context of a Taylor number $Ta = 4\Omega^2 h_T^4 / \nu^2 = (h_T / \delta_E)^4$, a measure of the relative importance of rotational and viscous forces. By examining the heat flux– Ta relationship for a range of Rayleigh numbers, Kelley deduced that convective heat fluxes are strongly inhibited for $Ta \gtrsim 10^3$. This is equivalent to $h_T / \delta_E > 5.6$ (Carpenter and Timmermans 2014), close to the transition value found here based on the LSA. The two transition values of h_T / δ_E may be similar because Ekman and thermal interfacial thicknesses are comparable between diffusive convection and thermal convection, where they both arise as boundary layers. A similar condition on the transition to the rotationally controlled regime in thermal convection was also proposed by King et al. (2012). As is shown in Fig. 4, the effect of salinity on the transition value of h_T / δ_E is nearly negligible: $(h_T / \delta_E)^4 = 4.0 \pm 0.2$ for a range of r and R_ρ . However, we note that the salinity stratification does affect stability properties of the staircase, as Ra_l^c is larger for larger R_ρ (Fig. 3b) and smaller r (Fig. 3c). We return to a comparison of Kelley's condition and our LSA-based condition for transition to rotationally controlled convection in section 3.

The LSA solutions can further provide physical insight into how rotation inhibits convection, which we describe next.

d. Physical process of stabilization by rotation

To understand how rotation stabilizes diffusive convection, it is useful to examine how vertical structures of the perturbation velocity and vorticity are affected. As we will show in the following analysis, the perturbation vertical velocity w_* is closely related to the perturbation horizontal vorticity. Given $\xi_* = \partial v_* / \partial x_* - \partial u_* / \partial y_*$ and $\partial w_* / \partial z_* = -(\partial u_* / \partial x_* + \partial v_* / \partial y_*)$, based on solutions for ξ_* and w_* [(18) and (19)], we can solve explicitly for u_* and v_* . For simplicity, we orient the horizontal coordinate so that the wavenumber in the y direction $l_* = 0$, and $k_* = K_*$, which yields

$$u_* = i \left(\frac{1}{K_*} \frac{\partial w_*}{\partial z_*} \right), \quad (25)$$

$$v_* = i \left(-\frac{1}{K_*} \xi_* \right). \quad (26)$$

Using these relations, we can express the y component of the horizontal vorticity $q_{y*} = \partial u_* / \partial z_* - \partial w_* / \partial x_*$, in terms of w_* as

$$q_{y*} = \frac{i}{K_*} \left(\frac{\partial^2 w_*}{\partial z_*^2} - K_*^2 w_* \right). \quad (27)$$

The vertical structures of perturbation quantities w_* , q_{y*} , and $(R_\rho S_* - T_*)$, for fixed values of Ra_l , R_ρ , H , and r , are shown in Figs. 5a,c. The density perturbation $(R_\rho S_* - T_*)$ is nondimensionalized by $\rho_0 \alpha \Delta T$ and first appears in (14). The mixed layer is in the upper part of the domain (only the top half of the domain is shown), and we approximate the unstable boundary layer to be the region below this whose upper and lower boundaries have vertical density gradients of 0.01 and 0, respectively (indicated by the gray bar in Fig. 5); the

stable interface core is below the unstable boundary layer. The maximum magnitude of each nondimensional perturbation variable is set to 3; phase relationships between perturbation variables are not retained. The corresponding linear growth rates σ_{r*} for rotating and nonrotating cases are 868 and 5322, respectively (i.e., rotation stabilizes the convection), and the corresponding horizontal wavenumbers K_* for rotating and nonrotating cases are 26.8 and 11.9, respectively (i.e., rotation increases the horizontal wavenumber of the most unstable mode).

In both rotating and nonrotating cases (Figs. 5a,c, respectively) we find that the vertical velocity perturbation w_* is focused in the unstable boundary layer where the background density gradient is negative, and extends only weakly into the stable interface core and the mixed layer. This is in agreement with previous studies which suggest that unstable boundary layers trigger convection (e.g., Linden and Shirtcliffe 1978; Carpenter et al. 2012b). The density perturbation $(R_\rho S_* - T_*)$ is confined to the interface region (i.e., the unstable boundary layer and the stable core) where the background density gradient is nonzero. It changes sign across the unstable boundary layer and the stable core, reflecting the change in sign of the background density gradient.

The y component of the horizontal vorticity perturbation q_{y*} and w_* share a similar vertical structure. This is because $K_* \gg 1$ and w_* is mainly composed of small vertical wavenumbers (i.e., n is small); the first term on the rhs of (27) is negligibly small, and q_{y*} is generally proportional to w_* . It is notable that q_{y*} (and also w_*) has a vertical extent in the presence of rotation that is significantly larger than without rotation. We can explore this by considering the governing equation for q_{y*} :

$$\frac{1}{Pr} \frac{\partial q_{y*}}{\partial t_*} = \nabla_*^2 q_{y*} + \frac{1}{Ek_l} \frac{\partial v_*}{\partial z_*} + Ra_l \frac{\partial (R_\rho S_* - T_*)}{\partial x_*}, \quad (28)$$

where the LHS represents the growth of q_{y*} , the first term on the rhs represents diffusion by molecular viscosity, the second term is a contribution from the tilting of planetary vorticity by vertical shear of the horizontal flow, and the third term is the baroclinic production term associated with the horizontal density gradient. The vertical structure of each term, normalized by the maximum amplitude of the baroclinic production term, is shown Figs. 5b and 5d.

The growth of q_{y*} follows the structure of q_{y*} being the largest in the unstable boundary layer. The largest term contributing to the growth of q_{y*} in the boundary layer is the baroclinic (buoyancy) production. Note that this term necessarily drops to zero in the mixed layer where the buoyancy perturbation is approximately zero (due to vanishing background density gradients). It also undergoes a sign change between the unstable boundary layer and the stable interface core. The viscous diffusion term dampens the growth of q_{y*} , which overall is a relatively minor effect. The stabilizing role of rotation can be seen in the boundary layer region of the rotating case (Fig. 5b) where the tilting of planetary vorticity is largely responsible for counteracting the baroclinic production that is solely responsible for producing growth (in the nonrotating case, and in the boundary

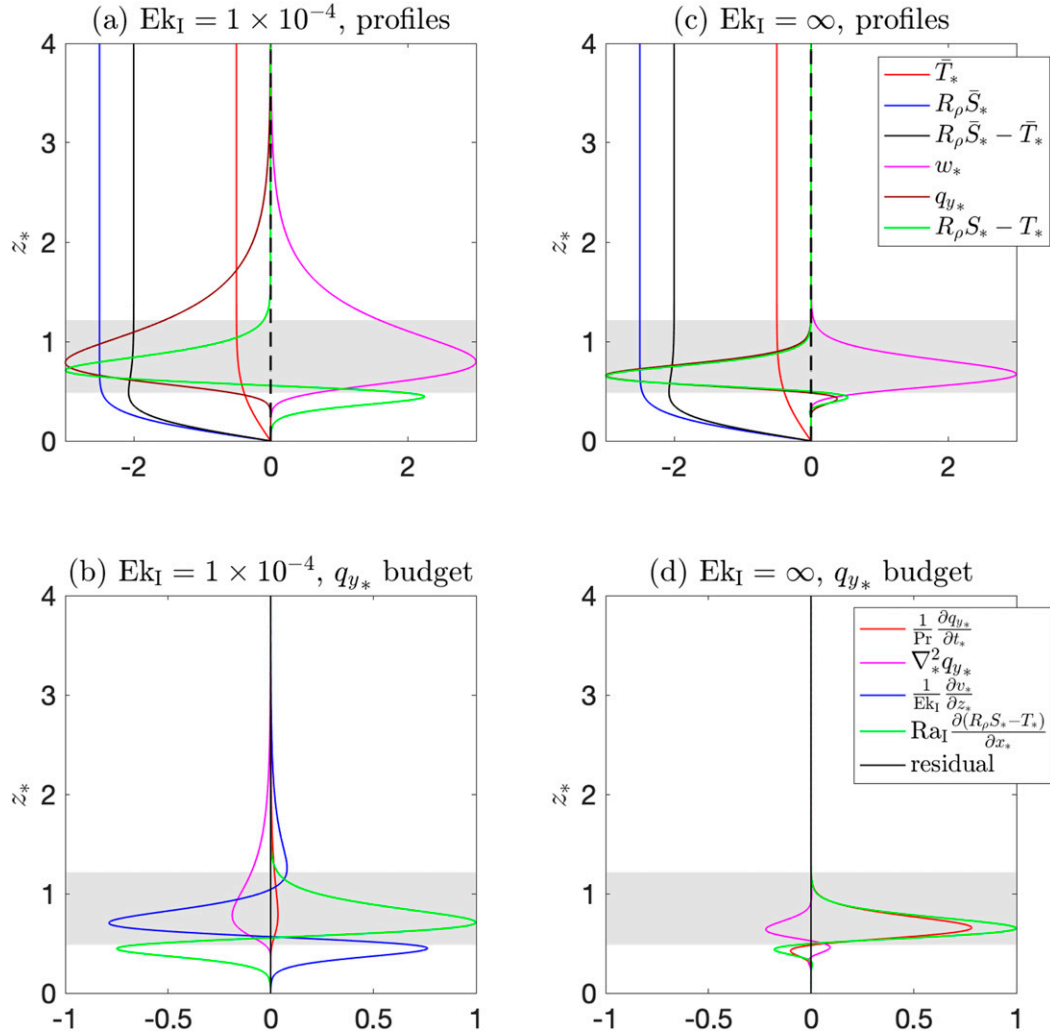


FIG. 5. Background temperature, salinity, and density profiles (relative to the reference state) and vertical structures of perturbation vertical velocity w_* , horizontal vorticity q_{y*} , and density $R_\rho S_* - T_*$ in the upper half of the domain ($z_* = 0-4$) for $Ra_I = 4 \times 10^7$, $R_\rho = 5$, $H = 10$, $r = 2$ and (a) $Ek_I = 10^{-4}$, (c) $Ek_I = \infty$. For illustration purposes the maximum magnitudes of w_* , q_{y*} and $R_\rho S_* - T_*$ have been set to 3. (b),(d) The vertical structures of each term in the horizontal vorticity budget for cases in (a) and (c), respectively. Terms have been normalized by the maximum magnitude of the baroclinic production term $Ra_I \partial(R_\rho S_* - T_*)/\partial x_*$. The gray bar indicates the unstable boundary layer, whose lower and upper boundaries have vertical gradient of background density (non-dimensionalized by $\rho_0 \alpha \Delta T/H$) equal to 0 and 0.01, respectively. Note that the planetary vorticity tilting term $[(1/Ek_I)(\partial v_*/\partial z_*)]$ vanishes in the absence of rotation in (d).

layer of the rotating case). It is interesting to note though that the tilting term contributes to growth in the stable interface core and the mixed layer, where it is largely counteracted by the baroclinic term and viscous term, respectively.

In summary, the growth of horizontal vorticity (q_{y*}) is largely confined to the unstable boundary layers through the baroclinic production term. When rotation is included we see the tilting of planetary vorticity providing a stabilization of this mechanism in the unstable boundary layer. As the vertical velocity perturbation (w_*) is generally proportional to q_{y*} , vertical motion of convection is therefore inhibited in the presence of rotation. Thus far, our LSA indicates rotation

suppresses diffusive–convective fluxes, and we have found a transition to the rotationally controlled regime that is consistent with the Kelley condition. Next, we test these predictions using DNS.

3. Direct numerical simulations

In this section, we perform two-dimensional (2D) DNS as well as a number of 3D DNS to explore the applicability of the linear stability transition criterion to finite amplitude turbulent convection. Beyond the transition, we expect the suppression of convection by rotation to yield smaller diffusive–convective

heat fluxes compared to the nonrotating case. Although double-diffusive convection is three-dimensional, 2D experiments have been shown to accurately simulate heat fluxes compared to their 3D counterparts (Flanagan et al. 2013; Hieronymus and Carpenter 2016). Our simulations solve the Boussinesq momentum equations, continuity equation and advection–diffusion equations assuming a linear equation of state. For the 2D experiments, variations in the y direction are set to 0. Periodic boundary conditions are applied at the side-walls of the domain. Periodic boundary conditions are also applied at the bottom and top boundaries, except with restoring such that the mean temperature and salinity differences across the domain do not change. The domain width to height ratio is set to 2 for 2D experiments and 1 or 0.5 for 3D experiments (we refer to this later); and the resolution is chosen such that the grid size is smaller than or approximately equal to twice the Batchelor scale given by $L_B = (\nu\kappa_s^2/\epsilon)^{1/4}$, where ϵ is the volume averaged kinetic energy dissipation rate (Carpenter et al. 2012a; Carpenter and Timmermans 2014); this ensures that the molecular diffusion of salt is properly simulated. For our simulations, we use the DEDALUS package which utilizes a spectral numerical method (Burns et al. 2020). Carpenter and Timmermans (2014) used a different numerical code (see Winters et al. 2004), and only conducted 2D experiments.

To begin, we perform a set of 2D experiments using the same parameters as the DNS experiments of Carpenter and Timmermans (2014) for comparison with their results. While for the LSA, we used interfacial Ekman and Rayleigh numbers (i.e., that depended on the thermal interfacial thickness), for the DNS we use Rayleigh and Ekman numbers that depend on the domain height \mathcal{H} : $Ra = g\alpha\Delta T\mathcal{H}^3/(\kappa_T\nu)$ and $Ek = \nu/(2\Omega\mathcal{H}^2)$. This is because the thermal interfacial thickness h_T varies over the course of a simulation. Following Carpenter and Timmermans (2014), we choose $R_\rho = (2, 5)$, $Ra = (6.5 \times 10^5, 3.3 \times 10^6, 1.6 \times 10^7)$ and $Ek = (\infty, 1 \times 10^{-2}, 1 \times 10^{-3}, 2 \times 10^{-4}, 1 \times 10^{-4})$. For $R_\rho = 5$ and $Ra = (6.5 \times 10^5, 3.3 \times 10^6)$, extra experiments are conducted for $Ek = 2.5 \times 10^{-3}$. For these experiments, we use a 1152×576 grid in the horizontal and vertical, respectively. We conduct an additional set of experiments with $Ra = 1 \times 10^8$ and a broader range of $R_\rho = (3, 5, 7)$. A resolution of 2880×1440 is used for the $R_\rho = 3$ simulation and 2048×1024 for $R_\rho = (5, 7)$. Note that in the Arctic Ocean, $Ra \approx 10^8$ – 10^9 , and \mathcal{H} (i.e., typical thickness of a layer in a staircase) is $O(1\text{--}5)$ m (Shibley et al. 2017), so that $Ek \approx 10^{-2}$ – 4×10^{-4} , taking $\delta_E \approx 10$ cm for laminar flows in the Arctic Ocean. Therefore, our simulations may be at least generally representative of the Arctic diffusive–convective staircases.

Finally, we perform a number of complimentary 3D experiments for $R_\rho = 5$, $Ra = 6.5 \times 10^5$, and $Ek = (1 \times 10^{-2}, 2.5 \times 10^{-3}, 1 \times 10^{-3})$ with a resolution of $192 \times 192 \times 192$ and a domain width to height ratio of 1; as well as for $R_\rho = 5$, $Ra = 3.3 \times 10^6$, and $Ek = (2.5 \times 10^{-3}, 1 \times 10^{-3}, 2 \times 10^{-4})$ with a resolution of $144 \times 144 \times 288$ and a domain width to height ratio of 0.5. Compared to the 2D experiments, the domain width to height ratio for the 3D experiments is reduced significantly due to limited computing resources, although we ensure that at least one convective cell is resolved in the domain.

All experiments have $Pr = 6.25$ and $\tau = 0.01$ (as used in the LSA). These values differ from those characterizing the Arctic Ocean (13 and 0.005, respectively) for which the simulations would be too computationally intensive for large Ra (1×10^8). While the simulated heat fluxes will differ from the Arctic setting, the choice of parameters will not affect validation of the LSA results.

All numerical experiments are initialized with $H = \mathcal{H}/h_T = 11$ and $r = h_T/h_S = 1$, with the initial temperature and salinity profiles taking the form specified in (17). Random noise is added to the temperature profile at the start of each simulation, which is integrated until the simulated staircase reaches quasi-equilibrium with respect to heat fluxes (we note that quasi-equilibrium was not attained for the three experiments with $Ra = 1 \times 10^8$ and $Ek = 1 \times 10^{-4}$, and refer to this later). Representative snapshots of the density field for a nonrotating and rotating simulation are shown in Fig. 6. The effect of rotation on the structure of double diffusive convection is qualitatively clear in these examples: when rotation is absent (Fig. 6a), there appears to be a single large convection cell on either side of the diffusive core. Under the influence of rotation (Fig. 6b), however, a number of distinct plumes are observed rising and sinking from the interface. It is clear that the most unstable mode has a larger horizontal wavenumber in the presence of rotation.

Of primary importance is quantifying how rotation affects diffusive convective heat fluxes F_H , and estimates of heat fluxes will allow us to test whether the nonrotating and rotating regimes found in the LSA apply. Here we calculate heat fluxes across the central isotherms of interfaces in the same manner as Winters and D’Asaro (1996) and Carpenter and Timmermans (2014). This diascalar heat flux (in dimensional form) is estimated by

$$F_H = \frac{\rho_0 c_p}{A} \int_s \kappa_T \nabla T \cdot \mathbf{n} ds, \quad (29)$$

where c_p is the specific heat capacity of water, \mathbf{n} is the unit vector normal to the central isotherm, ds is the length of integration along the central isotherm, and A is the horizontal width of the simulated domain. The central isotherm temperature is taken to be the average temperature of the entire system. For the 3D experiments, F_H is first calculated in each vertical (x – z direction) plane and averaged along the y direction. Note that considering averages of convective heat fluxes in the mixed layer returns values that only differ by about 1% from estimates inferred from (29) (see Carpenter and Timmermans 2014), although the convective heat fluxes have much larger temporal variation. Finally, it is useful to introduce the Nusselt number (Nu) which is a measure of the diascalar heat flux relative to the value for pure conduction:

$$Nu = \frac{F_H}{\frac{\rho_0 c_p \kappa_T}{\mathcal{H}} \Delta T}, \quad (30)$$

where ΔT is the temperature jump across the interface (equivalent to the temperature difference between the top and bottom of the domain).

Previous studies have suggested that when $R_\rho \gtrsim 2$, the thermal diffusive core is largely undisturbed and the fluid motion

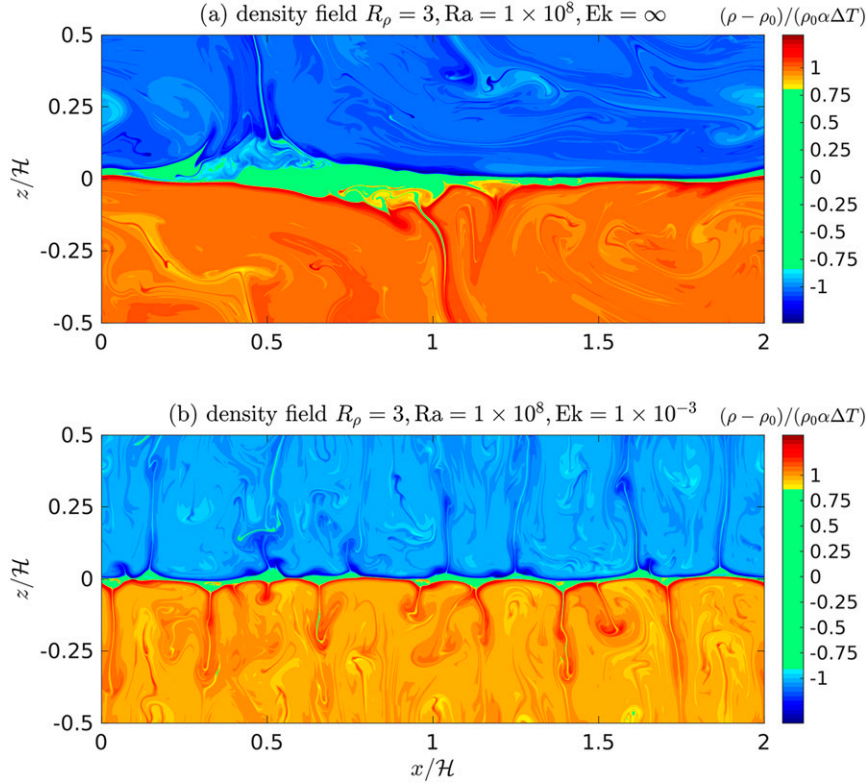


FIG. 6. Representative snapshots of the DNS density field for experiments with $R_\rho = 3$, $Ra = 1 \times 10^8$ and (a) $Ek = \infty$, (b) $Ek = 1 \times 10^{-3}$. A more organized convection is notable in the presence of rotation in (b).

there is laminar, so the diascalar heat flux can be well approximated to be $F_H \approx \rho_0 c_p \kappa_T \partial T / \partial z|_s$ (Linden and Shirtcliffe 1978; Carpenter et al. 2012a; Carpenter and Timmermans 2014). Considering $h_T = \Delta T / (\partial T / \partial z)|_s$ yields $Nu \approx \mathcal{H} / h_T$. Therefore, the transition to rotationally controlled heat fluxes stemming from Kelley, $h_T / \delta_E = 5.6$, is equivalently written as a transition Nusselt number of $Nu_{\text{Kelley}}^t = 0.18 Ek^{-1/2}$ (Carpenter and Timmermans 2014). Similarly, based on our LSA analysis, the transition occurs at $Nu_{\text{LSA}}^t = 0.25 Ek^{-1/2}$.

Average Nu versus $Ek^{-1/2}$ for all experiments are plotted in Fig. 7; for comparison, the corresponding simulation results of Carpenter and Timmermans (2014) are also shown (asterisks). For the three experiments with $Ra = 1 \times 10^8$ and $Ek = 1 \times 10^{-4}$, values of Nu did not reach quasi-equilibrium and were continuing to decrease at the end of the simulations. Open circles are used to indicate the final values of Nu attained for these experiments (Fig. 7), which represent only upper bound values. Two transition lines, indicating the Kelley and LSA transition conditions, are also plotted. The Nu remains largely unchanged as Ek is decreased from the nonrotating case (on the left side of the plot) toward $Ek = 0.01$ (i.e., $Ek^{-1/2} = 10$), in agreement with the LSA that weak rotation does not change the stability properties of the diffusive boundary layer. When Ek is reduced further (i.e., enhanced rotation), the results approach the two transition lines. Near this point, there is a relatively sharp increase in Nu , which has been suggested to be

caused by nonlinear Ekman transport in the thermal boundary layer forced by cyclonic circulation of convective plumes (e.g., Rossby 1969; Julien et al. 1996; King et al. 2012). After the transition lines are crossed, further reducing Ek completely shuts down convection, until heat transport is only pure conduction ($Nu = 1$).

To the left of the transition, the simulated Nu agrees reasonably well between 2D and 3D experiments (Fig. 7). The 3D-simulated Nu is generally larger than the 2D value, in part due to the reduced width to height ratio of the 3D domain. For the parameters of the simulation, we find that reducing the 2D domain width to height ratio by a factor of 1/2 or 1/4 yields an increase in Nu by $\sim 10\%$. After accounting for this effect, we find the 3D Nu to be $\sim 10\%$ larger than the 2D values, which may result from better resolving the convective cells. Closer to the transition, the simulated Nu is found to differ between the 2D and 3D experiments; after convection has completely shut down ($Nu = 1$) in the 2D experiments, convection remains active in the 3D experiments ($Nu > 1$). This may be due to the fact that the 3D-simulated Nu is generally larger than the 2D values (i.e., stronger convection) for the reasons noted above. Further reducing Ek yields $Nu = 1$ for both the 2D and 3D experiments.

We find the overall Nu – $Ek^{-1/2}$ relationship resembles the study of Carpenter and Timmermans (2014), which is now examined in a larger parameter space. Note the simulated Nu

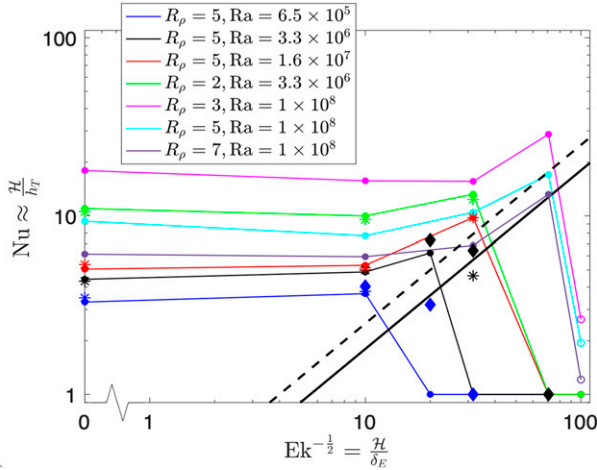


FIG. 7. The relationship between DNS quasi-equilibrium Nu with $Ek^{-1/2}$ for all simulations. The asterisks denote the quasi-equilibrium values of Nu from the 2D simulations of [Carpenter and Timmermans \(2014\)](#); circles denote results from 2D, and diamonds denote results from 3D simulations in the present study. Note a different numerical code was used by [Carpenter and Timmermans \(2014\)](#), see text. The solid circles indicate that 2D experiments have reached quasi-equilibrium while open circles indicate otherwise (i.e., they are only upper-bound values on quasi-equilibrium Nu). The black solid line and dashed line indicate the transition to a rotationally controlled regime predicted by the Kelley condition and our LSA-based condition, respectively. Note the rapid drop of Nu (suppression of heat fluxes) when the LSA-based transition line is crossed into the rotational regime on the right side of the plot except for the case $R_p = 7$, $Ra = 1 \times 10^8$ (see text).

for $R_p = 5$, $Ra = 3.3 \times 10^6$, and $Ek = 1 \times 10^{-3}$ in this study is different from that of [Carpenter and Timmermans \(2014\)](#). This result is close to the transition lines and may be sensitive to initial random noise and numerical methods. We find that the LSA-based condition gives a good estimation of the transition to a rotationally controlled regime, except when $R_p = 7$ and $Ra = 1 \times 10^8$. For this pair of parameters, Nu continues to increase after the LSA condition is crossed and does not decrease until the Kelley condition is crossed. This may be partly due to the fact that larger R_p and smaller H correspond to somewhat larger $(h_T/\delta_E)^f$ for the LSA-based condition (cf. [Fig. 4](#)), bringing it closer to the Kelley condition. For the other experiments, Nu immediately decreases after the LSA-based condition is crossed. The good agreement between the LSA-based transition criterion and DNS results suggests that the LSA captures the essential features of the stabilization of diffusive convection by rotation.

4. Summary and discussion

We have investigated how the linear stability properties, and heat fluxes, of a diffusive–convective staircase are affected by planetary rotation. Via LSA we have shown that rotation stabilizes convection by increasing the critical interfacial Rayleigh number, Ra_f^c , for its onset and reducing the growth rate of the most unstable mode. A $-4/3$ power law, $Ra_f^c \propto Ek_l^{-4/3}$, is found

when rotation strongly influences the flow for a range of values of H , R_p , and r . A transition from nonrotating to rotating diffusive convection is shown to occur for $h_T/\delta_E \approx 4.0$ (i.e., rotation is important when the thermal interfacial thickness is more than about 4 times the frictional Ekman layer thickness). This transition value is close to the Kelley condition, $h_T/\delta_E = 5.6$, which was originally formulated based on heat flux measurements of rotating (single-component) thermal convection experiments ([Rossby 1969](#); [Kelley 1987](#); [Carpenter and Timmermans 2014](#)). We suggest these two transition criteria are similar because for both thermal and diffusive convection, it is the unstable thermal boundary layer that triggers convection; the rotational effect is well quantified by comparing the Ekman and thermal interfacial thicknesses, as suggested by [King et al. \(2012\)](#). We find that the LSA results indicate the stabilizing effect of salinity has nearly negligible effect on the value of $(h_T/\delta_E)^f$ ([Fig. 4](#)).

Despite the generally good agreement between the Kelley and LSA transition criteria, there is no reason to expect they should be equal given the approximations and assumptions that have been made. For the LSA-based condition, we describe the background temperature and salinity profiles using error functions, which are an idealization of the actual structure of diffusive–convective interfaces. This is important because the stability boundary has been shown to be sensitive to the exact form of background density stratification ([Carpenter et al. 2012b](#)). Further, Ra_f^c is taken to be when σ_{r*} exceeds 2π . While this is only an approximate criterion; for the LSA to be valid, σ_{r*} should significantly exceed 2π if neglecting the time evolution of the background profiles by diffusion ([Smyth and Carpenter 2019](#)). Different thresholds of σ_{r*} will lead to different values of h_T/δ_E for the transition to the rotationally controlled regime. Finally, $(h_T/\delta_E)^f$ is determined by intersecting the fit of $Ra_f^c(Ek_l)$ in the rotationally controlled regime with the nonrotating value of Ra_f^c , when in fact the transition is a gradual and broad region of Ek_l ([Fig. 3](#)). In sum, both the Kelley and LSA-based criteria should be regarded as approximate, with some empirical refinement likely needed.

We have then investigated the physical mechanisms for the suppression of diffusive convection by rotation through an examination of the horizontal vorticity budget. In the absence of rotation, the horizontal density gradient effectively generates horizontal vorticity and drives vertical motion in the unstable boundary layer. In the presence of strong rotation, however, the tilting of planetary vorticity by vertical shear of the horizontal velocity strongly counteracts baroclinic production. As a result, the vertical motion of convection is strongly inhibited. Previous studies have usually referred to the Taylor–Proudman theorem as the mechanism for the stabilizing effects of rotation ([Chandrasekhar 1953, 2013](#); [Niiler and Bisshopp 1965](#)). The current analysis, however, offers a new perspective in understanding the effect of rotation.

To validate our LSA-based transition criterion, we have conducted a series of 2D DNS experiments as well as a number of complementary 3D experiments using a range of parameters consistent with past experiments and broadly applicable to diffusive–convective staircases in the Arctic

Ocean. For sufficiently large Ek ($Ek \geq 10^{-2}$), the nondimensional heat flux Nu is found to be largely unchanged compared to the nonrotating case. The Nu is generally found to decrease sharply after the LSA-based and Kelley conditions are crossed into the strongly rotating regime. We conclude that the LSA captures the essential features of the stabilization of diffusive convection by planetary rotation, and provides a theoretical framework for the transition. For staircases in the Arctic Ocean's Canadian Basin, thermal interfacial thicknesses are typically thinner than a few times the Ekman layer thickness, and planetary rotation should not influence heat fluxes (Carpenter and Timmermans 2014). On the other hand, staircases in the Eurasian Basin can have thermal interfacial thicknesses around 1 m (Shibley et al. 2017) and rotation may inhibit heat fluxes in these interfaces; see the discussion by Carpenter and Timmermans (2014).

Although we have used parameters in the LSA and DNS that resemble those of the Arctic Ocean's diffusive-convective staircases, the analysis method and revealed physical processes may be generalized to other diffusive-convective settings. The LSA can serve as an important tool to understand the effects of rotation on diffusive convection, which is especially useful for those systems characterized by large Rayleigh numbers, as it will require exceptional computing resources to conduct direct numerical simulations.

Acknowledgments. Y. Liang acknowledges discussions with Daniel Lecoanet, Zhongtian Zhang, and Nicole Shibley. M.-L. Timmermans acknowledges support from the National Science Foundation Division of Polar Programs under Award 1950077. J. R. Carpenter acknowledges the Helmholtz Association funding through the POF IV programme. We acknowledge high-performance computing support from the Center for Research Computing at Yale.

Data availability statement. Output for all DNS experiments is being deposited in the Dryad Digital Repository (<https://doi.org/10.5061/dryad.8sf7m0cmp>). Code for the linear stability analysis is available upon request.

REFERENCES

- Baines, P., and A. Gill, 1969: On thermohaline convection with linear gradients. *J. Fluid Mech.*, **37**, 289–306, <https://doi.org/10.1017/S0022112069000553>.
- Burns, K. J., G. M. Vasil, J. S. Oishi, D. Lecoanet, and B. P. Brown, 2020: Dedalus: A flexible framework for numerical simulations with spectral methods. *Phys. Rev. Res.*, **2**, 023068, <https://doi.org/10.1103/PhysRevResearch.2.023068>.
- Carmack, E., and Coauthors, 2015: Toward quantifying the increasing role of oceanic heat in sea ice loss in the new arctic. *Bull. Amer. Meteor. Soc.*, **96**, 2079–2105, <https://doi.org/10.1175/BAMS-D-13-00177.1>.
- Carpenter, J., and M.-L. Timmermans, 2014: Does rotation influence double-diffusive fluxes in polar oceans? *J. Phys. Oceanogr.*, **44**, 289–296, <https://doi.org/10.1175/JPO-D-13-098.1>.
- , T. Sommer, and A. Wüest, 2012a: Simulations of a double-diffusive interface in the diffusive convection regime. *J. Fluid Mech.*, **711**, 411–436, <https://doi.org/10.1017/jfm.2012.399>.
- , —, and —, 2012b: Stability of a double-diffusive interface in the diffusive convection regime. *J. Phys. Oceanogr.*, **42**, 840–854, <https://doi.org/10.1175/JPO-D-11-0118.1>.
- Chandrasekhar, S., 1953: The instability of a layer of fluid heated below and subject to Coriolis forces. *Proc. Roy. Soc. London*, **A217**, 306–327, <https://www.jstor.org/stable/99187>.
- , 2013: *Hydrodynamic and Hydromagnetic Stability*. Courier Corporation, 652 pp.
- Flanagan, J. D., A. S. Leffler, and T. Radko, 2013: Heat transport through diffusive interfaces. *Geophys. Res. Lett.*, **40**, 2466–2470, <https://doi.org/10.1002/grl.50440>.
- Guthrie, J. D., I. Fer, and J. Morison, 2015: Observational validation of the diffusive convection flux laws in the Amundsen Basin, Arctic Ocean. *J. Geophys. Res. Oceans*, **120**, 7880–7896, <https://doi.org/10.1002/2015JC010884>.
- Hieronymus, M., and J. R. Carpenter, 2016: Energy and variance budgets of a diffusive staircase with implications for heat flux scaling. *J. Phys. Oceanogr.*, **46**, 2553–2569, <https://doi.org/10.1175/JPO-D-15-0155.1>.
- Julien, K., S. Legg, J. McWilliams, and J. Werne, 1996: Rapidly rotating turbulent Rayleigh-Bénard convection. *J. Fluid Mech.*, **322**, 243–273, <https://doi.org/10.1017/S0022112096002789>.
- Kelley, D. E., 1987: The influence of planetary rotation on oceanic double-diffusive fluxes. *J. Mar. Res.*, **45**, 829–841, <https://doi.org/10.1357/002224087788327136>.
- , 1990: Fluxes through diffusive staircases: A new formulation. *J. Geophys. Res.*, **95**, 3365–3371, <https://doi.org/10.1029/JC095iC03p03365>.
- King, E., S. Stellmach, and J. Aurnou, 2012: Heat transfer by rapidly rotating Rayleigh-Bénard convection. *J. Fluid Mech.*, **691**, 568–582, <https://doi.org/10.1017/jfm.2011.493>.
- Linden, P., and T. Shirtcliffe, 1978: The diffusive interface in double-diffusive convection. *J. Fluid Mech.*, **87**, 417–432, <https://doi.org/10.1017/S002211207800169X>.
- Neal, V. T., S. Neshyba, and W. Denner, 1969: Thermal stratification in the Arctic Ocean. *Science*, **166**, 373–374, <https://doi.org/10.1126/science.166.3903.373>.
- Neshyba, S., V. T. Neal, and W. Denner, 1971: Temperature and conductivity measurements under ice island T-3. *J. Geophys. Res.*, **76**, 8107–8120, <https://doi.org/10.1029/JC076i033p08107>.
- Nield, D., 1967: The thermohaline Rayleigh-Jeffreys problem. *J. Fluid Mech.*, **29**, 545–558, <https://doi.org/10.1017/S0022112067001028>.
- Niiler, P. P., and F. E. Bisshopp, 1965: On the influence of Coriolis force on onset of thermal convection. *J. Fluid Mech.*, **22**, 753–761, <https://doi.org/10.1017/S002211206500112X>.
- Padman, L., and T. M. Dillon, 1987: Vertical heat fluxes through the Beaufort Sea thermohaline staircase. *J. Geophys. Res.*, **92**, 10 799–10 806, <https://doi.org/10.1029/JC092iC10p10799>.
- Pearlstein, A. J., 1981: Effect of rotation on the stability of a doubly diffusive fluid layer. *J. Fluid Mech.*, **103**, 389–412, <https://doi.org/10.1017/S0022112081001390>.
- Polyakov, I. V., J. E. Walsh, and R. Kwok, 2012: Recent changes of Arctic multiyear sea ice coverage and the likely causes. *Bull. Amer. Meteor. Soc.*, **93**, 145–151, <https://doi.org/10.1175/BAMS-D-11-00070.1>.
- Radko, T., 2013: *Double-Diffusive Convection*. Cambridge University Press, 342 pp.
- Rossby, H., 1969: A study of Bénard convection with and without rotation. *J. Fluid Mech.*, **36**, 309–335, <https://doi.org/10.1017/S0022112069001674>.
- Schmitt, R. W., 1994: Double diffusion in oceanography. *Annu. Rev. Fluid Mech.*, **26**, 255–285, <https://doi.org/10.1146/annurev.fl.26.010194.001351>.

- Shibley, N. C., M.-L. Timmermans, J. R. Carpenter, and J. M. Toole, 2017: Spatial variability of the Arctic Ocean's double-diffusive staircase. *J. Geophys. Res. Oceans*, **122**, 980–994, <https://doi.org/10.1002/2016JC012419>.
- Smyth, W. D., and J. R. Carpenter, 2019: *Instability in Geophysical Flows*. Cambridge University Press, 328 pp.
- Sommer, T., J. R. Carpenter, M. Schmid, R. G. Lueck, M. Schurter, and A. Wüest, 2013: Interface structure and flux laws in a natural double-diffusive layering. *J. Geophys. Res. Oceans*, **118**, 6092–6106, <https://doi.org/10.1002/2013JC009166>.
- , —, and A. Wüest, 2014: Double-diffusive interfaces in Lake Kivu reproduced by direct numerical simulations. *Geophys. Res. Lett.*, **41**, 5114–5121, <https://doi.org/10.1002/2014GL060716>.
- Stern, M. E., 1960: The “salt-fountain” and thermohaline convection. *Tellus*, **12**, 172–175, <https://doi.org/10.3402/tellusa.v12i2.9378>.
- Timmermans, M.-L., J. Toole, R. Krishfield, and P. Winsor, 2008: Ice-tethered profiler observations of the double-diffusive staircase in the Canada basin thermocline. *J. Geophys. Res. Oceans*, **113**, C00A02, <https://doi.org/10.1029/2008JC004829>.
- Turner, J., 1965: The coupled turbulent transports of salt and heat across a sharp density interface. *Int. J. Heat Mass Transfer*, **8**, 759–767, [https://doi.org/10.1016/0017-9310\(65\)90022-0](https://doi.org/10.1016/0017-9310(65)90022-0).
- , and H. Stommel, 1964: A new case of convection in the presence of combined vertical salinity and temperature gradients. *Proc. Natl. Acad. Sci. USA*, **52**, 49–53, <https://doi.org/10.1073/pnas.52.1.49>.
- Veronis, G., 1965: On finite amplitude instability in thermohaline convection. *J. Mar. Res.*, **23**, 1–17.
- Winters, K. B., and E. A. D’Asaro, 1996: Diascalar flux and the rate of fluid mixing. *J. Fluid Mech.*, **317**, 179–193, <https://doi.org/10.1017/S0022112096000717>.
- , J. MacKinnon, and B. Mills, 2004: A spectral model for process studies of rotating, density-stratified flows. *J. Atmos. Oceanic Technol.*, **21**, 69–94, [https://doi.org/10.1175/1520-0426\(2004\)021<0069:ASMFPS>2.0.CO;2](https://doi.org/10.1175/1520-0426(2004)021<0069:ASMFPS>2.0.CO;2).